Ultra-High-Responsivity Broadband Detection of Si Metal–Semiconductor–Metal Schottky Photodetectors Improved by ZnO Nanorod Arrays

Dung-Sheng Tsai,[†,‡] Chin-An Lin,[†] Wei-Cheng Lien,[†,§] Hung-Chih Chang,[†] Yuh-Lin Wang,[‡] and Jr-Hau He[†,*]

[†]Institute of Photonics and Optoelectronics, and Department of Electrical Engineering, National Taiwan University, Taipei, Taiwan, [‡]Institute of Atomic and Molecular Sciences, Academia Sinica, Taipei, Taiwan, and [§]Berkeley Sensor and Actuator Center, University of California, Berkeley, California, United States

ABSTRACT This study describes a strategy for developing ultra-high-responsivity broadband Si-based photodetectors (PDs) using ZnO nanorod arrays (NRAs). The ZnO NRAs grown by a low-temperature hydrothermal method with large growth area and high growth rate absorb the photons effectively in the UV region and provide refractive index matching between Si and air for the long-wavelength region, leading to 3 and 2 orders of magnitude increase in the responsivity of Si metal–semiconductor–metal PDs in the UV and visible/NIR regions, respectively. Significantly enhanced performances agree with the theoretical analysis based on the finite-difference time-domain method. These results clearly demonstrate that Si PDs combined with ZnO NRAs hold high potential in next-generation broadband PDs.

KEYWORDS: ZnO · nanorod · nanowire · antireflection · photodetector · photodiode

Si-based photodetectors (PDs) in the forms of Schottky diodes, p–n diodes, p–i–n diodes, and back-to-back Schottky metal–semiconductor–metal (MSM) PDs are widely used owing to their monolithic integratibility with low-cost complementary metal-oxide-semiconductor technology.[1] Among them, MSM PDs exhibit attractive applications in optoelectronic integration circuits with advantages such as planar device structure, easy fabrication processes, and fast response. The broadband PDs have been carried out with III–V semiconductors, organic semiconductors/inorganic nanocrystals, and carbon nanotubes/organic semiconductors/C_{60}.[2–4] With the advantages of CMOS-compatible processing and reduced cost, the Si-based broadband detectors are highly desirable.[4] Considering the optical sensitivity of Si, the Si PDs have some performance limitations, such as low peak quantum efficiency and relatively weak spectral responses in UV (<400 nm) and near-infrared (NIR) wavelength (>700 nm) regions. The lack of UV response associated with the limited UV penetration depth imposes a crucial limitation in Si PD applications to astronomical detection and atmospheric and space remote sensing.[5] The weak photoresponse in the NIR region together with the interference fringes in the long-wavelength response due to Fabry–Perot resonance leads to the insufficient NIR sensitivity, limiting Si PDs to imaging applications.[6,7]

To boost the responsivity by reducing the surface reflection, most PDs are provided with antireflection coatings (ARCs).[8,9] Typically, a single-layer ARC is made by a quarter wavelength (λ/4) dielectric layer, *e.g.*, MgF_2, SiN, TiO_2, ZnO, or ZnS.[10] However, the λ/4 ARC works only at a specific incident angle and a single incident wavelength via the destructive interference of waves reflected from the top and the bottom of the ARC.[11] Recently the availability of nanofabrication has enabled the engineering of materials with desired antireflective characteristics.[8,10,12–20] For example, antireflective nanostructures based on the effect of zero-order grating were fabricated by etching techniques.[13–16] Despite the superior antireflective properties, the resulting surface defect states created by etching processes could degrade the performance of devices. Moreover, Schubert *et al.* reported that nanostructured multilayers as an ARC with a tailored refractive index profile can be made using oblique sputtering.[8,10] However, the more complicated the fabrication used to improve the desired properties, the higher the production cost. Recently ZnO nanostructures also demonstrated exciting possibilities for next-generation ARCs to suppress the Fresnel reflection effectively.[12,21,22] Despite the many investigations on fabrications and optical characterizations of nanostructure-based ARCs, more practical device

* Address correspondence to jhhe@cc.ee.ntu.edu.tw.

Received for review January 24, 2011 and accepted September 25, 2011.

Published online September 26, 2011
10.1021/nn203357e

© 2011 American Chemical Society

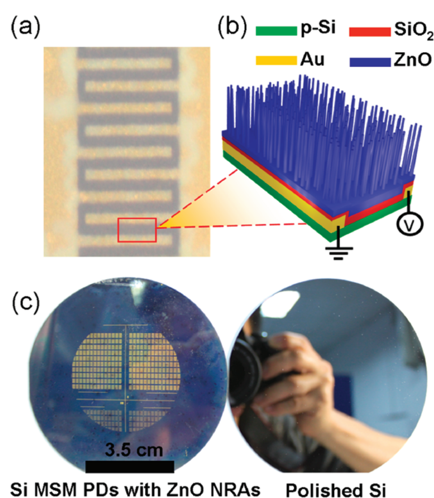

Figure 1. (a) Optical microscopic top-view image, (b) schematic of the Si MSM PD with ZnO NRAs, and (c) wafer-scale photographs of the Si MSM PDs with ZnO NRAs and polished Si.

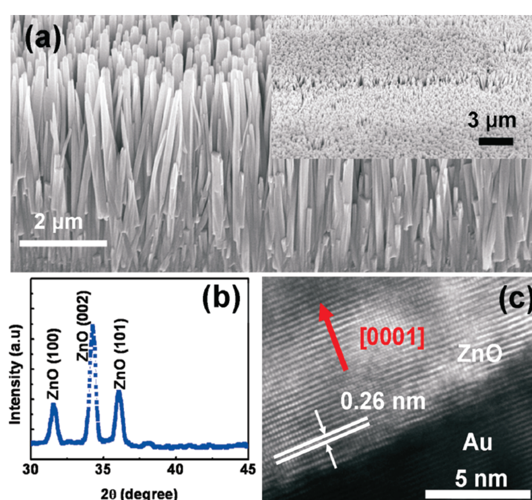

Figure 2. (a) Cross-sectional SEM image of the as-grown ZnO NRAs on Si MSM PDs, (b) XRD pattern of as-grown ZnO NRAs on Si MSM PDs, and (c) HRTEM image of the single ZnO nanorod grown on Au electrodes. The inset in (a) is the low-magnification SEM image of ZnO NRAs on the Si MSM PD surface with a tilt angle of 45° with respect to the normal of the sample.

applications are needed to demonstrate their feasibility. Moreover, one should note that ZnO nanowires also exhibit ultrahigh UV sensitivity (for ~pW level light detection) due to their special semiconducting, photonic, and piezoelectric properties and pronounced surface effects.[23]

In this study, we demonstrated Si MSM PDs with ZnO nanorod arrays (NRAs) as a top layer, which absorbs the UV photons (photon energy > band gap of ZnO) effectively and serves as an ARC layer, providing an effective refractive-index gradient between Si and air in the long-wavelength region (photon energy < band gap of ZnO), enabling broadband detection with greatly enhanced responsivity. The responsivity of Si MSM PDs is increased by up to 3 orders of magnitude in the UV region and by 2 orders of magnitude in the visible/NIR regions due to ZnO NRA layers. The huge enhancement of broadband detection by Si MSM PDs with ZnO NRAs could allow the low-cost production of photonic devices and extend the application potential for Si-based optoelectronic devices.

RESULTS AND DISCUSSION

An optical microscopic image, a schematic of the Si MSM PD with ZnO NRA ARCs, and a photograph of the samples with large area (4-in. wafer), *i.e.*, Si MSM PDs with ZnO NRAs and polished Si wafer, are depicted in Figure 1. As shown in Figure 1c, we demonstrate that the large-scale ZnO NRAs can be grown on the p-Si substrate using hydrothermal methods, and the Si wafer with ZnO NRA/Si PDs exhibits a gray color due to the lower reflectance of ZnO NRAs, while the polished one exhibits a clear reflected image. SiO_2 layers of 100 nm thickness were deposited on Si MSM PDs before the ZnO NRA growth. SiO_2 as a passivation layer can reduce the leakage current effectively since the ZnO nanorods are not an insulating material owing to a lot of intrinsic oxygen defects on the surface.[24] As shown in Figure S1 in the Supporting Information, the dark current can be decreased by up to 2 orders of magnitude under 15 V bias with the presence of SiO_2 passivation layers. Figure 2a is a cross-sectional scanning electron microscopy (SEM) image of the NRAs on the Si MSM PDs, showing that large-scale, well-aligned ZnO NRAs were successfully grown on the Si MSM PDs by the hydrothermal approach. The density, diameter, and length of the ZnO NRAs on the Si MSM PDs are approximately 1.6×10^9 cm^{-2}, 110 nm, and 4.5 μm, respectively. The X-ray diffraction (XRD) spectrum of Si MSM PDs with ZnO NRAs in Figure 2b shows that all peaks are indexed as a hexagonal wurtzite ZnO structure. The high-resolution transmission electron microscopy (HRTEM) image of a single ZnO nanorod, as shown in Figure 2c, indicates that the ZnO NRAs are single crystalline and grow along the [0001] direction. It has been reported that among various growth methods of ZnO nanostructures, ZnO nanorods/nanowires with high crystal quality can be grown perpendicularly on any surface of devices/substrates using the hydrothermal method with advantages such as low-temperature process, large-area growth, and high growth rate.[25]

In order to highlight the enhancement of the photoresponse using ZnO NRAs, conventional Si MSM PDs were fabricated without ZnO NRAs as a comparison. Figure 3 shows the current−voltage (*I*−*V*) characteristics of the pristine Si MSM PDs and Si MSM PDs with ZnO NRAs measured in the dark and under 543 nm He−Ne laser illumination (photon energy = 2.3 eV) with a power density of 4.1×10^2 w/m^2. Under 15 V bias, the photocurrent to dark current contrast ratio of

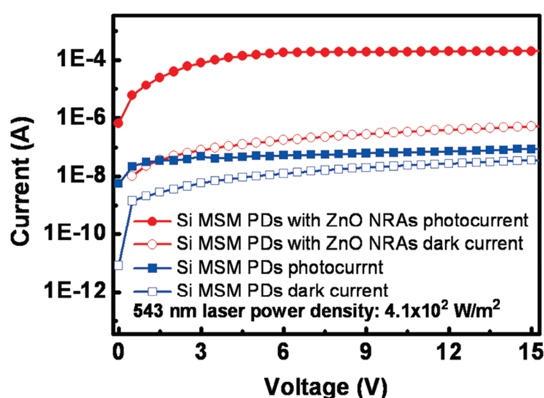

Figure 3. *I*−*V* characteristics of the Si MSM PDs with and without ZnO NRAs measured in the dark and under 543 nm illumination. The light power density is 4.1 × 10^2 w/m^2.

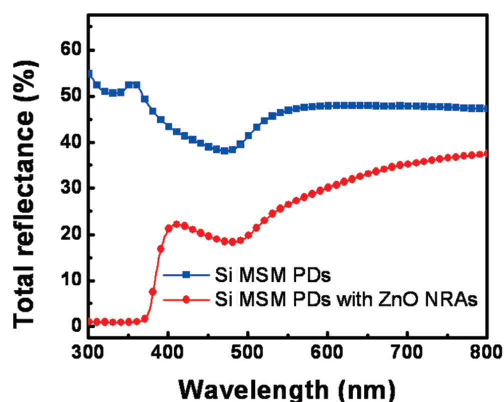

Figure 4. Reflectance spectra of Si MSM PDs with and without ZnO NRAs.

Si MSM PDs is increased from 2.5 to 380 by introducing ZnO NRA layers. Note that the green light at 543 nm is not absorbed by wide-band-gap ZnO (3.3 eV at room temperature). In other words, the photocurrent enhancement of Si MSM PDs is due to the fact that the antireflective ZnO NRA structures guide the photons efficiently to create more opportunities for generating the photocurrent in Si MSM PDs.

To further confirm the antireflective characteristics of ZnO NRAs, the total reflection spectra were measured, as shown in Figure 4. ZnO NRAs drastically reduce the reflection over a wide range of wavelengths. The reflectance of Si MSM PDs with ZnO NRAs is decreased to below 1% in the UV region and 35% in the visible/NIR regions due to the strong band gap absorption of ZnO NRAs in the UV region and the graded effective refractive index profile of the NRA layers in the visible/NIR regions, which will be stated as follows. When the energy of the incident photons is near or larger than the band gap energy of ZnO, the reflection in the UV region is related with band gap absorption of ZnO, leading to the flat and low reflection spectra. As the wavelength of incident light is above 368 nm (lower than the band gap of ZnO), the imaginary part of the refractive index of ZnO is negligible, and thus ZnO is nonabsorbing.[26] Due to the length variation of NRAs and the tapering shape of NRA tips, the filling factor (the area ratio of NRs to the total substrate surface) of the NRAs increases with the depth, leading to a gradual decrease of effective refractive index from the surface of Si MSM PDs to the air based on the effective medium theory.[8,12,15,21,27] The refractive index gradient causes the incident light to be reflected at different depths in ZnO NRA layers, where the light waves with different phases partially or wholly cancel one another through destructive interferences, giving rise to the broadband antireflective characteristics in the visible/NIR regions.

In order to reveal the light propagation nature across the interfaces, the steady-state distribution of electromagnetic fields within the PD structures was simulated by finite-difference time-domain (FDTD) analysis based on Maxwell's equations, which are used to calculate the propagation of the electromagnetic wave. For FDTD simulation, the simplified PD structures are available in Figure S2 in the Supporting Information. Figure 5a−c visualize the time-averaged TE-polarized electric field intensity ($|E_z|$) distribution within Si MSM PDs at 543 nm. All calculated values are normalized to the ones of the excitation source. The insets of Figure 5a−c, where the region of Si surfaces is enlarged, show that the nanorods, separated by air gaps, not only help light propagate across the interfaces by avoiding the abrupt index transition from air to Si but also widen the field distribution within the device by increasing the light scattering on the surface. The space charge region width in our Si PDs for 15 V bias is about 1.20 μm using $W = [2\varepsilon_s(V_{bi} + V_R)/eN_d]^{1/2}$, where the permittivity is $\varepsilon_s = 1.04 \times 10^{-12}$ F/cm, the built-in potential is $V_{bi} = 0.67$ V, the reverse-bias voltage is $V_R = 15$ V, and the doping concentration is $N_d = 1.40 \times 10^{16}$ cm^{-3}.[28] In order to detect the optical power in the space charge region in Si PDs, we set the detector at 0.6 μm below the surface of Si in the simulation. Figure 5d shows the optical power of TE-polarized light detected at 0.6 μm below the surface of Si as a function of time in bare Si MSM PDs, Si MSM PDs with ZnO films, and Si MSM PDs with ZnO NRAs. The steady-state power values at 543 nm for the bare Si MSM PDs, Si MSM PDs with ZnO films, and Si MSM PDs with ZnO NRAs are 0.49, 0.57, and 0.65, respectively, indicating that ZnO NRA layers can increase the number of photons reaching the light absorption regions and thus the possibility for generating photocurrents, which agrees with the *I*−*V* enhancement under 543 nm illumination seen in Figure 3. Similar results of TM-polarized magnetic field intensity ($|H_z|$) distributions are available in Figure S3a, S3b, and S3c in the Supporting Information. The steady-state power values of TM-polarized light at 543 nm detected at 0.6 μm below the surface of bare Si MSM PDs, Si MSM PDs with ZnO films, and Si MSM PDs with ZnO NRAs are 0.45, 0.48, and 0.53, respectively, as indicated in Figure S3d in the Supporting Information, demonstrating the importance of antireflective ZnO NRA layers as well.

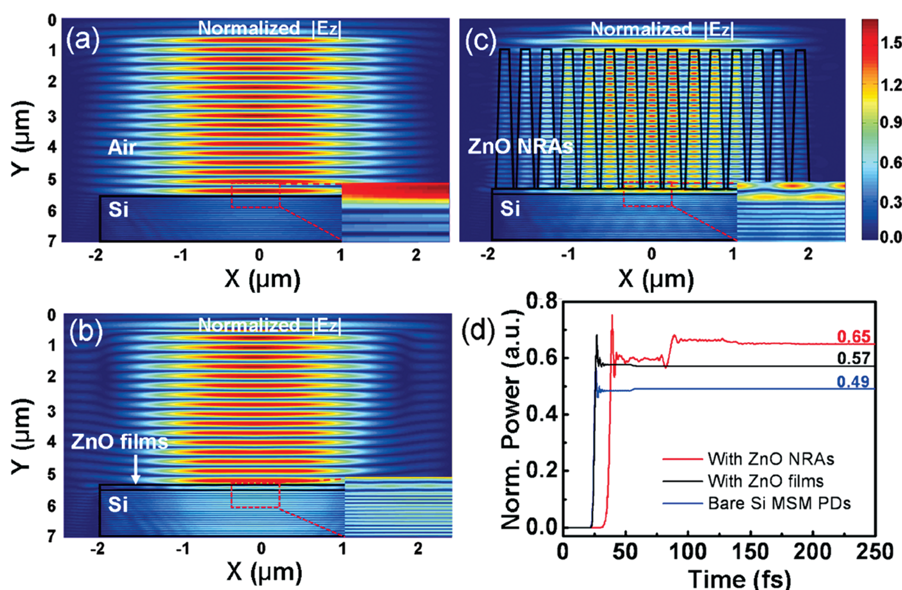

Figure 5. Time-averaged and normalized TE electric field, $|E_z|$, distribution at 543 nm simulated by FDTD analysis (a) within the bare Si MSM PDs, (b) with ZnO films, and (c) with ZnO NRAs. (d) Normalized optical power, detected at 0.6 μm below the surface of Si, as a function of time. The insets in (a)–(c) are the enlarged images at the top Si surface.

To evaluate the spectral photoresponse, the Si MSM PDs with ZnO NRAs were characterized by measuring the responsivity in the spectral range from 300 to 800 nm under the bias of 15 V, as shown in Figure 6. In addition to using a pristine Si MSM PD as a direct comparison, we also had a control device by just applying 100-nm-thick layers of ZnO. Except for the difference in morphologies between ZnO NRAs and ZnO layers, the two PDs were fabricated using the same process flow. One can see that there are distinct spectral responses. Pristine Si MSM PDs achieve poor UV and NIR responses. A significantly improved photoresponse of the Si MSM PDs with ZnO NRAs from UV to NIR regions indicates that the ZnO NRAs can not only enhance the responsivity of Si MSM PDs but also extend the detection region from UV to NIR. The responsivity of Si MSM PDs is enhanced by over 2 orders of magnitude in the visible/NIR regions by ZnO NRAs. Surprisingly, the responsivity is increased by up to 3 orders of magnitude in the UV region due to the introduction of ZnO NRAs. One should note that the nanostructured Si PDs were fabricated by various etching techniques.[29,30] Despite their superior AR properties, the resulting surface defect states created by the etching process reduce the performance of nanostructured Si PDs, restricting their practical applications in optoelectronics. Moreover, the nanostructured Si PDs still exhibit a weak sensitivity of UV detection due to the physical limitations of Si.

As compared with those with ZnO NRAs, Si MSM PDs with 100-nm-thick ZnO layers show a similar ability in UV regions but poor ability to detect visible/NIR light, distinguishing Si MSM PDs with ZnO NRAs as ultrahigh-responsivity broadband PDs. The authors suggest

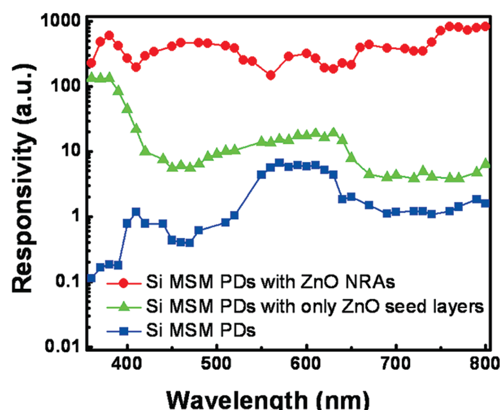

Figure 6. Comparison of the spectral responsivity under 15 V bias.

that the significant enhancement of broadband responsivity can occur *via* two distinct mechanisms operating in different spectral regions (above and below the band gap energy of ZnO). As the energy of the incident photons is much lower than the band gap energy of ZnO, more photons collected at the depletion region of the p-Si/Au through the antireflective ZnO NRAs contribute to the responsivity enhancement in visible/NIR regions. The comparisons of the responsivity spectra of Si MSM PDs with ZnO NRAs to Si MSM PDs with only 100-nm-thick ZnO layers in visible/NIR regions reveal the importance of the morphology on antireflective performances. As incident photon energy is higher than the band gap energy of ZnO, the incident photons can penetrate only a limited depth near the air/ZnO interface. Accordingly, the ultrahigh UV responsivity of Si MSM PDs with ZnO NRAs is related with the band gap absorption of ZnO, which is also

supported by the flat and low reflectance in the UV region in Figure 4. The ultrahigh UV responsivity of Si MSM PDs with 100-nm-thick ZnO layers close to that with ZnO NRAs also confirms the above rationale.

Note that the responsivity of Si MSM PDs in the UV region can be increased with ZnO NRAs even though there is an insulating SiO_2 layer between semiconducting ZnO and metallic Au electrodes. The reasons are discussed as follows. Metal–insulator–semiconductor (MIS)-based PDs, such as the ZnO metal–insulator–semiconductor–insulator–metal (MISIM) UV PDs and ITO/SiO_2/GaN MIS UV PDs, exhibit the enhanced photocurrent to dark-current contrast ratios due to the reduced leakage current by adding the SiO_2 passivation layers.[31,32] Moreover, H. Zhu *et al*. reported that the responsivity of Au/MgO/MgZnO MIS structure UV PDs can be improved *via* the carrier multiplication process in the insulating MgO layer.[33] As shown in Figure S4 in the Supporting Information, the thickness of the SiO_2 layer is only approximately 50 nm at the sidewall of Au contact. The estimated electric field in the SiO_2 layer is 1.5×10^6 V/cm at 15 V bias using $E = V/d$, where E is the electric field, V is the bias voltage, and d is the thickness of the SiO_2 layers. Under such high intensity of the electric field on the relatively thin SiO_2 layer, the UV photogenerated carriers can tunnel through the SiO_2 layer.[33–35]

For the ultrahigh broadband responsivity, we conclude that when the light is illuminated on Si MSM PDs with ZnO NRAs, the electron–hole pairs are mainly generated in Si and ZnO NRAs by low-energy and high-energy photons, respectively.[36] The generated carriers drift toward the electrodes because of the applied electric field. The seemingly efficient broadband photoresponse from Si MSM PDs with ZnO NRAs suggests that the ZnO NRAs not only guide photons effectively as an antireflective nanostructure in the long-wavelength regions but also absorb photons as an effective photoconductor in the short-wavelength regions. It is worth noting that ZnO nanostrucutures exhibit a UV photoconductive gain as high as 10^8.[25–30,37–42] We believe that the growth of ZnO NRAs for Si MSM PDs is not fully optimized. More works on the optimization of length variation and shape of ZnO NRAs to the responsivity are currently under investigation.

CONCLUSION

In summary, Si MSM PDs with ZnO NRAs exhibit ultrahigh broadband responsivity, while the responsivity in the UV and NIR regions was relatively weak for pristine Si MSM PDs. ZnO NRAs absorb the UV photons effectively in the short-wavelength region and provide impedance matching between Si and air through an effective index gradient to facilitate more photons getting into the PDs in the long-wavelength region, leading to ~3 and ~2 orders of magnitude increase in the responsivity of Si MSM PDs in the UV and visible/NIR regions, respectively. This study demonstrates that Si MSM PDs incorporating ZnO NRAs hold promise for potential applications in the next-generation broadband PDs.

METHODS

The MSM PDs adopted Au electrodes with interdigitated fingers on the p-type Si(100) substrate with a resistivity of 1–100 Ωcm using photolithography, as shown in Figure 1. The 200-nm-thick Au fingers were designed to be 8 μm wide and 150 μm long with 8-μm-wide spacing and were deposited by electron beam evaporation to serve as Schottky contacts. Au contacts were annealed at 600 °C under N_2 ambient with the rapid thermal anneal process for 30 s. The active area of the whole device was $250 \times 158\ \mu m^2$. A 100-nm-thick SiO_2 passivation layer was deposited on Si MSM PDs using plasma-enhanced chemical vapor deposition, followed by the deposition of a 100-nm-thick ZnO seed layer using radio frequency (rf) magnetron sputter deposition with a rf power of 40 W and a working pressure of 5 mTorr under a flow of Ar gases. ZnO NRAs were grown in aqueous solution containing zinc nitrate hexahydrate ($Zn(NO_3)_2$, 10 mM) and ammonia (NH_4OH) solution at 95 °C for 2 h.

After the growth process, the resulting products were collected for phase identification using XRD with a fixed incident angle of 0.5°. A morphological study of ZnO nanostructures has been carried out with a JEOL JSM-6500 field emission SEM. Microstructure analysis was investigated using a JEOL 2100 HRTEM operating at 200 kV. The reflection spectra were measured with a JASCO V-670 UV–visible spectrometer in the spectral range from 300 to 800 nm. The Keithley 4200-SCS semiconductor characterization system and the EQE-R3011 (Enli Technology Co., Ltd.) spectral response system were used to measure I–V characteristics and responsivity of the fabricated PDs.

For FDTD simulation, the grid sizes are $\Delta x \times \Delta y = 0.01 \times 0.02\ \mu m^2$ in the space domain, and the time step is $\Delta t = 0.024$ fs in the time domain. The boundaries in x and y directions are surrounded by the perfectly matching 0.5 μm layers to absorb the electromagnetic waves.[43] The electrode in the PD structure is neglected in FDTD simulation. The excitation source, with the same width (4 μm) as that of the simulated device structure, is placed at 5.5 μm from the upper boundary of the interface of Si. For the Si PDs with ZnO NRAs, the number of nanorods on the surface is decided by the linear density (d_L) of the ZnO NRAs, which can be obtained by the relationship $d_L = d_A^{1/2}$, where $d_A = 1.6 \times 10^9$ cm^{-2} is the area density of ZnO NRAs estimated from SEM images.

Acknowledgment. This research was supported by the National Science Council Grant Nos. 99-2622-E-002-019-CC3, 99-2112-M-002-024-MY3, and 99-2120-M-007-011.

Supporting Information Available: The I–V measurements highlight SiO_2 passivation layers to reduce the leakage current of Si MSM PDs with ZnO NRAs effectively. For FDTD simulation, simplified PD structures and simulation results of TM-polarized magnetic field intensity ($|H_z|$) distributions are available. The thickness of SiO_2 layers and definition of sidewall step coverage are shown in the cross-sectional SEM image. This material is available free of charge via the Internet at http://pubs.acs.org.

REFERENCES AND NOTES

1. Razeghi, M.; Rogalski, A. Semiconductor Ultraviolet Detectors. *J. Appl. Phys.* **1996**, *79*, 7433–7473.
2. Arnold, M. S.; Zimmerman, J. D.; Renshaw, C. K.; Xu, X.; Lunt, R. R.; Austin, C. M.; Forrest, S. R. Broad Spectral Response Using Carbon Nanotube/Organic Semiconductor/C_{60} Photodetectors. *Nano Lett.* **2009**, *9*, 3354–3358.
3. McDonald, S. A.; Konstantatos, G.; Zhang, S. G.; Cyr, P. W.; Klem, E. J. D.; Levina, L.; Sargent, E. H. Solution-Processed PbS Quantum Dot Infrared Photodetectors and Photovoltaics. *Nat. Mater.* **2005**, *4*, 138–1424.
4. People, R.; Bean, J. C.; Bethea, C. G.; Sputz, S. K.; Peticolas, L. J. Broadband (8−14 μm), Normal Incidence, Pseudomorphic Ge_xSi_{1-x}/Si Strained-Layer Infrared Photodetector Operating between 20 and 77 K. *Appl. Phys. Lett.* **1992**, *61*, 1122–1124.
5. Choi, J.-M.; Im., S. Ultraviolet Enhanced Si-Photodetector Using p-NiO Films. *Appl. Surf. Sci.* **2005**, *244*, 435–438.
6. Groom, D. E.; Holland, S. E.; Levi, M. E.; Palaio, N. P.; Perlmutter, S.; Stover, R. J.; Wei, M. Quantum Efficiency of a Back-Illuminated CCD Imager: An Optical Approach. *Proc. SPIE* **1999**, *3649*, 80–90.
7. Bai, Y.; Bernd, S. G.; Mosack, J. R.; Farris, M. C.; Montroy, J. T.; Bajaj, J. Hybrid CMOS Focal Plane Array with Extended UV and NIR Response for Space Applications. *Proc. SPIE* **2004**, *5167*, 83–93.
8. Xi, J. Q.; Schubert, M. F.; Kim, J. K.; Schubert, E. F.; Chen, M.; Lin, S. Y.; Liu, W.; Smart, J. A. Optical Thin-Film Materials with Low Refractive Index for Broadband Elimination of Fresnel Reflection. *Nat. Photonics* **2007**, *1*, 176–179.
9. Dobrowolski, J. A.; Poitras, D.; Ma, P.; Vakil, H.; Acree, M. Toward Perfect Antireflection Coatings: Numerical Investigation. *Appl. Opt.* **2001**, *41*, 3075–3083.
10. Chhajed, S.; Schubert, M. F.; Kim, J. K.; Schubert, E. F. Nanostructured Multilayer Graded-Index Antireflection Coating for Si Solar Cells with Broadband and Omnidirectional Characteristics. *Appl. Phys. Lett.* **2008**, *93*, 251108.
11. Zhou, W.; Tao, M.; Chen, L.; Yang, H. Microstructured Surface Design for Omnidirectional Antireflection Coatings on Solar Cells. *J. Appl. Phys.* **2007**, *102*, 103105.
12. Chao, Y. C.; Chen, C. Y.; Lin, C. A.; Dai, Y. A.; He, J. H. Antireflection Effect of ZnO Nanorod Arrays. *J. Mater. Chem.* **2010**, *20*, 8134–8138.
13. Xu, H. B.; Lu, N.; Qi, D. P.; Hao, J. Y.; Gao, L. G.; Zhang, B.; Chi, L. F. Biomimetic Antireflective Si Nanopillar Arrays. *Small* **2008**, *4*, 1972–1975.
14. Sun, C. H.; Jiang, P.; Jiang, B. Broadband Moth-Eye Antireflection Coatings on Silicon. *Appl. Phys. Lett.* **2008**, *92*, 61112.
15. Wang, H. P.; Lai, K. Y.; Lin, Y. R.; Lin, C. A.; He, J. H. Periodic Si Nanopillar Arrays Fabricated by Colloidal Lithography and Catalytic Etching for Broadband and Omnidirectional Elimination of Fresnel Reflection. *Langmuir* **2010**, *26*, 12855–12858.
16. Lin, Y. R.; Wang, H. P.; Lin, C. A.; He, J. H. Surface Profile-Controlled Close-Packed Si Nanorod Arrays for Self-Cleaning Antireflection Coatings. *J. Appl. Phys.* **2009**, *106*, 114310.
17. Fan, Z.; Kapadia, R.; Leu, P.; Zhang, X.; Chueh, Y. L.; Takei, K.; Yu, K.; Jamshidi, A.; Rathore, A.; Ruebusch, D.; *et al.* Ordered Arrays of Dual-Diameter Nanopillars for Maximized Optical Absorption. *Nano Lett.* **2010**, *10*, 3823–3827.
18. Chueh, Y. L.; Fan, Z.; Takei, K.; Ko, H.; Kaoadia, R.; Rathore, A. A.; Miller, N.; Yu, K.; Wu, M.; Haller, E. E.; *et al.* Black Ge Based on Crystalline/Amorphous Core/Shell Nanoneedle Arrays. *Nano Lett.* **2010**, *10*, 520–523.
19. Lin, Y. R.; Lai, K. Y.; Wang, H. P.; He, J. H. Slope-Tunable Si Nanorod Arrays with Enhanced Antireflection and Self-Cleaning Properties. *Nanoscale* **2010**, *2*, 2765–2768.
20. Dai, Y. A.; Chang, H. J.; Lai, K. Y.; Lin, C. A.; Chung, R. J.; Lin, G. R.; He, J. H. Subwavelength Si Nanowire Arrays for Self-Cleaning Antireflection Coatings. *J. Mater. Chem.* **2010**, *20*, 10924–10930.
21. Lee, Y. J.; Ruby, D. S.; Peters, D. W.; Mckenzie, B. B.; Hsu, J. W. P. ZnO Nanostructures as Efficient Antireflection Layers in Solar Cells. *Nano Lett.* **2008**, *8*, 1501–1505.
22. Huang, J. H.; Chen, C. Y.; Lai, Y. F.; Shih, Y. I.; Lin, Y. C.; He, J. H.; Liu, C. P. Large-Area Oblique-Aligned ZnO Nanowires Through a Continuously Bent Columnar Buffer: Growth, Microstructure, and Antireflection. *Cryst. Growth Des.* **2010**, *10*, 3297–3301.
23. Yang, Q.; Guo, X.; Wang, W.; Zhang, Y.; Xu, S.; Lien, D. H.; Wang, Z. L. Enhancing Sensitivity of a Single ZnO Micro-/Nanowire Photodetector by Piezo-Phototronic Effect. *ACS Nano* **2010**, *4*, 6285–6291.
24. He, J. H.; Chang, P. H.; Chen, C. Y.; Tsai, K. T. Electrical and Optoelectronic Characterization of a ZnO Nanowire Contacted by Focused-Ion-Beam-Deposited Pt. *Nanotechnology* **2009**, *20*, 135701.
25. Wang, Z. L. ZnO Nanowire and Nanobelt Platform for Nanotechnology. *Mater. Sci. Eng., R* **2009**, *64*, 33–71.
26. Yoshikawa, H.; Adachi, S. Optical Constants of ZnO. *Jap. J. Appl. Phys.* **1997**, *36*, 6237–6243.
27. Rayleigh, J. S. On Reflection of Vibrations at the Confines of Two Media Between Which the Transition is Gradual. *Proc. London Math. Soc.* **1880**, *11*, 51–56.
28. Neamen, D. A. Semiconductor Physics and Devices, 3rd ed.; McGraw Hill Publications: New York, 2003; p 330.
29. Bae, J.; Kim, H.; Zhang, X. M.; Dang, C. H.; Zhang, Y.; Choi, Y. J.; Nurmikko, A.; Wang, Z. L. Si Nanowire Metal-Insulator-Semiconductor Photodetectors as Efficient Light Harvesters. *Nanotechnology* **2010**, *21*, 95502.
30. Huang, Z.; Carey, J. E.; Liu, M.; Guo, X.; Mazur, E.; Campbell, J. C. Microstructured Silicon Photodetector. *Appl. Phys. Lett.* **2006**, *89*, 33506.
31. Ali, G. M.; Chakrabarti, P. ZnO-Based Interdigitated MSM and MISIM Ultraviolet Photodetectors. *J. Phys. D: Appl. Phys.* **2010**, *43*, 415103.
32. Chiou, Y. Z.; Su, Y. K.; Chang, S. J.; Gong, J.; Chang, C. S.; Liu, S. H. The Properties of Photo Chemical-Vapor Deposition SiO_2 and Its Application in GaN Metal-Insulator Semiconductor Ultraviolet Photodetectors. *J. Electron. Mater.* **2002**, *32*, 395–399.
33. Zhu., H.; Shan, C. X.; Wang, L. K.; Zheng, J.; Zhang, J. Y.; Yao, B.; Shen, D. Z. Metel-Oxide-Semiconductor-Structure MgZnO Ultraviolet Photodetector with High Internal Gain. *J. Phys. Chem. C* **2010**, *114*, 7169–7172.
34. Griffiths, D. J. *Introduction to Electrodynamics*, 3rd ed.; Prentice Hall International Editions: NJ, 2003; p 104.
35. Lin, C. H.; Liu, C. W. Metal-Insulator-Semiconductor Photodetectors. *Sensors* **2010**, *10*, 8797–8826.
36. Lee, J. Y.; Choi, Y. S.; Yeom, W. H.; Yoon, Y. K.; Kim, J. H.; Im, S. Characterization of Films and Interfaces in n-ZnO/p-Si Photodiodes. *Thin Solid Films* **2002**, *420*, 112–116.
37. He, J. H.; Ho, C. H.; Chen, C. Y. Polymer Functionalized ZnO Nanobelts as Oxygen Sensors with a Significant Response Enhancement. *Nanotechnology* **2009**, *20*, 65503.
38. Lao, C. S.; Park, M. C.; Kuang, Q.; Deng, Y. L.; Sood, A. K.; Polla, D. L.; Wang, Z. L. Giant Enhancement in UV Response of ZnO Nanobelts by Polymer Surface-Functionalization. *J. Am. Chem. Soc.* **2007**, *129*, 12096–12097.
39. Chen, M. W; Chen, C. Y.; Lien, D. H.; Ding, Y.; He, J. H. Photoconductive Enhancement of Single ZnO Nanowire Through Localized Schottky Effects. *Opt. Express* **2010**, *18*, 14836–14841.
40. Zhai, T. Y.; Fang, X. S.; Liao, M. Y.; Xu, X. J.; Zeng, H. B.; Yoshio, B.; Golberg, D. A Comprehensive Review of One-Dimensional Metal-Oxide Nanostructure Photodetectors. *Sensors* **2009**, *9*, 6504–6529.
41. Soci, C.; Zhang, A.; Xiang, B.; Dayeh, S. A.; Aplin, D. P. R; Park, J.; Bao, X. Y.; Lo, Y. H.; Wang, D. L. ZnO Nanowire UV Photodetectors with High Internal Gain. *Nano Lett.* **2007**, *7*, 1003–1009.
42. Chen, C. Y.; Chen, M. W.; Ke, J. J.; Lin, C. A.; Retamal, J. R. D.; He, J. H. Surface Effects on Optical and Electrical Properties of ZnO Nanostructures. *Pure Appl. Chem.* **2010**, *82*, 2055–2077.
43. Berenger, J. P. A Perfectly Matched Layer for the Absorption of Electromagnetic−Waves. *J. Comput. Phys.* **1994**, *114*, 185–200.